Microelectromechanical Systems for Nanomechanical Testing: Electrostatic Actuation and Capacitive Sensing for High-Strain-Rate Testing

C. Li[1], D. Zhang[1,2], G. Cheng[1], Y. Zhu[1,*]

[1] Department of Mechanical and Aerospace Engineering, North Carolina State University, Raleigh, North Carolina 27695, USA

[2] College of Mechanical and Electrical Engineering, Zhengzhou University of Light Industry, Zhengzhou, Henan 450002, China

E-mail: yong_zhu@ncsu.edu

Abstract

There have been relatively few studies on mechanical properties of nanomaterials under high strain rates, mainly due to the lack of suitable nanomechanical testing devices. Here we present a new on-chip microelectromechanical system (MEMS) for high strain-rate nanomechanical testing (with strain rate up to 200 s^{-1}). The MEMS device consists of a fast-response electrostatic comb drive actuator, two capacitive displacement sensors and a load cell. The dynamic responses of the device in air and in vacuum are systematically modeled under both alternating and ramping forces. Two methods, capacitive readout and high-speed imaging, are used to measure the dynamic displacements, which agree well with the modeling results. While the attainable strain rate of the device is about 200 s^{-1}, it is interesting to find that the capacitive readout used in this work can only measure strain rate up to 22 s^{-1} due to its limit in bandwidth. To demonstrate the general capability of the new device, gold nanowires are tested at strain rates of 10^{-5} and 10 s^{-1} inside a scanning electron microscope. Increasing strain rate is found to yield higher yield strength and larger ductility.

1. Introduction

With rapid advances in nanotechnology in the past decades, a plethora of nanomaterials with outstanding material properties have been developed and a number of nanomaterial-enabled applications have emerged. One-dimensional (1D) nanomaterials are among the most important building blocks for these nano-enabled applications. For example, metal nanowires have been widely used in flexible, stretchable and wearable electronics applications such as touch panels, solar cells, wearable sensors, soft actuators and deformable antennas[1-3]. The operation and reliability of these device applications call for a thorough understanding of mechanical behaviors of the nanowires.

Mechanical behaviors of nanowires have been extensively investigated through atomistic simulations. More experimental investigations have been emerged recently as a result of advances in novel experimental methods[4-6]. Many interesting mechanical behaviors of nanowires have been reported, including ultrahigh strength[7-9], size-dependent elasticity[10-12], and dislocation nucleation from free surfaces[13,14]. A number of interesting rate- (or time-) dependent phenomena have been reported, such as stress relaxation and creep[15,16], recoverable plasticity[15,17], Bauschinger effect[15,17], brittle-to-ductile transition[18,19], and anelasticity[20]. However, most of the nanomechanical testing was conducted quasi-statically; dynamic testing especially high strain-rate testing of nanowires remains an area largely unexplored. It is in great need to conduct high strain-rate testing since nanowires especially metal nanowires can behave differently at high strain rates[21,14,19], which is of relevance to applications where these 1D nanomaterials are subject to high-rate loadings.

It is challenging to conduct high strain-rate nanomechanical testing since the apparatus must have an actuator with fast actuation speed and sensors with short response time. Microelectromechanical system (MEMS) has been widely used for nanomechanical testing[22-25] and might provide a solution to the high strain-rate testing. Naraghi et al.[26,27] reported testing polymer nanofibers with strain rate up to 200 s^{-1} using a MEMS-based load sensor and an external piezoelectric actuator. The external actuator provided the fast actuation, while force and displacement were measured from high-speed optical images using digital image correlation (DIC). However, this off-chip actuation method adds complexity for in-situ scanning or transmission electron microscope (SEM/TEM) testing and might be challenging in handling smaller samples such as nanowires (with diameters generally less than 100 nm).

As for the on-chip method, the strain rate attained so far has been quite limited, typically less than 10^{-1} s^{-1} [14,21]. Ramachandramoorthy et al.[19] reported high strain rate tensile testing of silver nanowires (up to 2 s^{-1}) using an on-chip MEMS thermal actuator. While the capacitive load sensor responded quickly, the thermal actuator limited the actuation speed due to the relatively slow heat transfer process. Nevertheless 2 s^{-1} is the largest strain rate that has been reported for tensile testing of nanowires. For metallic nanowires surface dislocation nucleation is the dominant deformation mechanism, which has been recently shown to exhibit pronounced temperature and strain rate dependence[13,14]. It is of important relevance to experimentally investigate how higher strain rate can impact dislocation nucleation and interactions, hence mechanical behavior of nanowires. A potential solution is to employ other types of MEMS actuators that can respond faster.

In this paper, we systematically investigated the dynamic response of a MEMS-based nanomechanical testing device with an electrostatic actuator and a capacitive sensor in air and inside SEM (near vacuum environment). The goal is to explore the maximum actuation speed and maximum strain rate attainable. The structure and operating principle of the device is first described. Analytical dynamic model is built to thoroughly investigate the device's response to AC actuation force and ramping force. Dynamic responses of the device are measured in air and in vacuum and compared well with the modeling results. The maximum strain rate that the device can attain is then discussed based on the modeling and experiment results. It is found that this device is able to achieve strain rate up to 200 s^{-1}; however, the capacitive readout can only measure strain rate up to 22 s^{-1} due to its limit in bandwidth. Finally, two gold nanowires are tested at strain rates of 10^{-5} s^{-1} and 10 s^{-1} in SEM to demonstrate the general capability of the device for high strain-rate nanomechanical testing.

2. Device Description

The MEMS devices were fabricated at MEMSCAP (Durham, NC) using the Silicon-on-Insulator Multi-User MEMS Process. Figure 1 shows a SEM image, schematic and lumped mechanical model of the MEMS device. The device consists of a comb-drive actuator, two displacement sensors (A and B) and a folded beam load cell (sensor). The central shuttle of the device is supported by four beams. A specimen is to be placed across the gap between Sensor B and the fixed anchor. Elongation of the specimen is simply determined by the displacement of Sensor B. If the damping force in Sensor B is negligible (*e.g.*, under quasi-static loading), then force in the specimen is equal to elongation of the load cell (displacement difference between Sensors A and B) multiplied by the stiffness of the load cell

because forces in the specimen and the load cell are equal (two springs connected in series). The dynamic force measurement will be discussed later. Stress and strain of the specimen can be calculated given the specimen's gauge length and cross-sectional area.

The configuration used here, similar to that of Tsuchiya et al.[28], is different from most MEMS-based nanomechanical testing devices where a specimen is placed between the actuator and the load cell. The current configuration eliminates the specimen rigid body motion due to the load cell displacement, which makes tracking the specimen deformation easier during *in-situ* testing. In addition, with this configuration, strain rate of the specimen can simply be defined by

$$\dot{\varepsilon} = \frac{1}{l_0}\frac{\partial d_B}{\partial t} \tag{1}$$

where d_B is the displacement of Sensor B, $\frac{\partial d_B}{\partial t}$ is the velocity of Sensor B, and l_0 is the gauge length of the specimen.

The actuator used in this work is an electrostatic comb-drive actuator. Compared to other types of actuators such as electrothermal actuator[29,30], comb-drive actuator can provide a constant force under a constant actuation voltage regardless of the travel distance and with no heating effect. The actuation force is proportional to the actuation voltage square as given by[31]

$$F_A = N_A \varepsilon \left(\frac{h}{g}\right) V^2 \tag{2}$$

where N_A is the number of pairs of comb fingers, ε is the permittivity, h is the thickness of the MEMS structure, g is the lateral gap between comb fingers, and V is the actuation voltage.

Both sensors (A and B) are the differential capacitive sensors, which can provide a quasi-

linear relationship[32,33] between displacement d and capacitance difference ΔC, *viz*.,

$$\Delta C = N_S \varepsilon A \left(\frac{1}{g_1 - d} - \frac{1}{g_1 + d}\right) \approx 2N\varepsilon A \frac{d}{g_1} \tag{3}$$

where N_S is the number of pairs of parallel plates, A is the overlapping area of two adjacent plates, and g_1 is the initial gap between the fixed plate and the closer movable plate.

3. Modeling

Based on the lumped mechanical model shown in Figure 1c, equations of motion of the device can be written as

$$m_A \ddot{d}_A + c_A \dot{d}_A + k_{SB} d_A + k_{LC}(d_A - d_B) = F_A \tag{4}$$

$$m_B \ddot{d}_B + c_B \dot{d}_B + k_S d_B - k_{LC}(d_A - d_B) = 0 \tag{5}$$

where m_A is the total mass of the moving portion of Sensor A and the actuator, m_B is the mass of the moving portion of Sensor B, d_A and d_B are the displacements of m_A and m_B, respectively, k_{SB}, k_{LC} and k_S are the stiffness of the supporting beams, load cell and specimen, respectively, and c_A and c_B are the damping coefficients with respect to m_A and m_B, respectively.

3.1 Dynamic response under AC actuation force: vacuum and air

For a linear system, dynamic response under AC actuation force (or frequency response) of the system can be characterized by its transfer function. In order to find out transfer function of this MEMS device, a state-space model was constructed based on the aforementioned equations of motion, *viz*.,

$$\dot{\boldsymbol{X}} = A\boldsymbol{X} + Bu \tag{6}$$

$$y = C\boldsymbol{X} \tag{7}$$

where state vector $\boldsymbol{X} = \begin{bmatrix} d_B \\ \dot{d}_B \\ d_A \\ \dot{d}_A \end{bmatrix}$, state matrix $A = \begin{bmatrix} 0 & 1 & 0 & 0 \\ -\frac{k_{LC}+k_S}{m_B} & -\frac{c_B}{m_B} & \frac{k_{LC}}{m_B} & 0 \\ 0 & 0 & 0 & 1 \\ \frac{k_{LC}}{m_A} & 0 & -\frac{k_{LC}+k_{SB}}{m_A} & -\frac{c_A}{m_A} \end{bmatrix}$, input matrix $B = \begin{bmatrix} 0 \\ 0 \\ 0 \\ \frac{1}{m_A} \end{bmatrix}$, and input $u = F_A$. Here only the displacement of Sensor B is chosen as the output since it is directly related to the specimen elongation, hence output $\mathrm{y} = d_{\mathrm{B}}$ and output matrix $C = [1 \quad 0 \quad 0 \quad 0]$. The system transfer function is then written as

$$G(s) = C(sI - A)^{-1}B$$

$$= \frac{k_{LC}}{m_A m_B s^4 + (c_A m_B + c_B m_A)s^3 + \left(c_A c_B + k_{SB} m_B + k_S m_A + k_{LC}(m_A + m_B)\right)s^2 + c_B(k_{LC} + k_{SB})s + c_A(k_{LC} + k_S)s + k_S k_{SB} + k_{LC} k_S + k_{LC} k_{SB}} \tag{8}$$

where $s = \boldsymbol{j}\omega$ with ω as the angular frequency, and I is the identity matrix. In Eq. 8, m_A = 1.68×10^{-8} kg and m_B = 5.99×10^{-9} kg, k_{SB} = 107 N/m, and k_{LC} = 850 N/m. Supporting beam stiffness and load cell stiffness were estimated by finite element analysis based on the measured dimensions using SEM. k_S is zero when there is no specimen mounted.

In vacuum, the damping coefficients c_A and c_B are treated to be approximately zeros, neglecting the intrinsic damping. With all the system parameters known, transfer function of the device in vacuum can be calculated using Eq. 8. Figure 2 plots bode magnitude plot of the device, which characterizes the relationship between the angular frequency ω of the input force F_A and the magnitude of the output displacement d_{B} with respect to displacement at $\omega = 0$. Since the system has two degrees of freedom, two peaks can be found corresponding to two undamped frequencies at resonance, ω_1 = 72,193 rad/s and ω_2 = 440,997 rad/s. Note that without damping, the magnitude approaches infinite at the natural frequencies.

In air, the damping effect needs to be considered. The damping coefficients c_A and c_B must be known in order to characterize the dynamic response of the device under AC actuation force. The two natural frequencies in air, ω_3 and ω_4, are expected to be smaller than their counterparts in vacuum if the device is underdamped in air. The damping coefficients of the device in air will be determined through experiments as described in Section 4.2 and theoretical calculation in Section 6.2.

3.2 Dynamic response under ramping actuation force: vacuum and air

To attain a constant strain rate in the specimen, i.e., constant velocity of Sensor B, a ramping force $F_A = \xi t$ is chosen as the input to the device, where the loading rate ξ is a constant.

In vacuum, the damping coefficients are zeros, hence the device model is simplified to a two-coupled-mass-spring system [34]. The system transient output $d_B(t)$ has the following form

$$d_B(t) = \frac{\xi t}{k_{SB}} - a_1 \xi \, sin(2\pi f_1 t) + a_2 \xi \, sin(2\pi f_2 t) \quad (9)$$

where a_1 and a_2 are constants that can be calculated with the known system parameters (*e.g.*, m_A, m_B, k_{SB}, k_{LC}) (both independent of ξ), and f_1 and f_2 are the two natural frequencies of the system in vacuum as identified in Section 3.1 ($\omega = 2\pi f$). $\frac{\xi}{k_{SB}}$ is defined as the nominal loading velocity. The output form of this two-coupled-mass-spring system is similar to that of a single-mass-spring system (see Appendix), but has to be solved numerically. The analytical solution of the single-mass-spring system can shed some light on the two-coupled-mass-spring system (i.e. the present device). The same goes for the single-mass-spring-damper system (see below). As shown in Eq. 9, $d_B(t)$ is the

superposition of a linear displacement $\frac{\xi t}{k_{SB}}$ and two sinusoidal displacements, which is schematically shown in Figure 3a. The linear displacement is the ideal displacement of Sensor B to achieve a constant strain rate in the specimen. The two sinusoidal displacements can be considered as deviation from the ideal linear displacement. Magnitude of the deviation is proportional to ξ. When ξ is small, the deviation is negligible, which is the case for quasi-static loading. However, this does not hold when ξ is large.

In air, considering the damping effect, the device model becomes a two-coupled-mass-spring-damper system. The system transient output $d_B(t)$ has the following form

$$d_B(t) = \frac{\xi t}{k_{SB}} - a_3\xi - a_4\xi e^{-a_5 t} sin(2\pi f_3 t + a_6) + a_7\xi e^{-a_8 t} sin(2\pi f_4 t + a_9) \quad (10)$$

where a_3 to a_9 are constants (a_5 and a_8 are positive) that can be calculated with the known system parameters (*e.g.*, m_A, m_B, k_{SB}, k_{LC}, c_A, c_B) (all independent of *s*), and f_3 and f_4 are the two natural frequencies of the system in air. The form is again similar to that of a single-mass-spring-damper system (see Appendix). Displacement d_B contains a linear term $\frac{\xi t}{k_{SB}}$ (the ideal displacement), a constant offset term $a_3\xi$, and two attenuated sinusoidal terms. Here the sum of the last three terms is the deviation with a magnitude also proportional to ξ. Figure 3b shows schematically the displacement $d_B(t)$ in this case.

4. Experiments

Dynamic responses of the device were measured experimentally under AC actuation and ramping actuation. Two methods were employed to measure displacement – optical imaging and capacitance readout. The responses in air, under both AC actuation and ramping actuation, were measured by the optical imaging, while the response in vacuum under ramping actuation was measured by the capacitive readout. The purpose of the response

under AC actuation is to validate the theory in Section 3.1 and obtain damping coefficients.

To image the displacement under dynamic testing, a high-speed camera (Phantom v4.3 with maximum frame rate 95,000 fps) was integrated to a Nikon LV150N optical microscope (at 1000× magnification), as shown in Figure 4. A light source (SOLA SE II 365) was used to provide strong white light needed for the high-speed imaging.

Recorded images were then processed using an image correlation method to obtain displacement. The method used here is based on the shift theorem of discrete Fourier transformation (DFT)[35]. First, a series of optical images were taken recording the motion of Sensor B or position of Sensor B at different moments (Figure 5a). Subsequently the images were cropped to the same region of interest – some parallel beams connected to the shuttle which is a periodic pattern as marked by red rectangle in Figure 5a. For each cropped image, the gray value of pixels in each column was averaged to produce a 1D periodic pixel intensity profile (Figure 5b), which was then analyzed using DFT (Figure 5c). Since displacement in spatial domain (Figure 5b) corresponds to phase shift in frequency domain (Figure 5c), the phase of the fundamental frequency which is the spatial frequency of the periodic pattern was recorded for each image and phase shift between images was then converted back to the spatial domain to calculate the displacement. A fixed periodic structure can also be chosen as the region of interest (green rectangle in Figure 5a) to serve as reference, whose displacement can be subtracted from the displacement of the moving structure to remove common motion induced noises such as vibration.

When compared with other displacement measurement techniques based on image processing, such as the commonly used DIC, this single frequency-based DFT method has

the advantage that it is less affected by image noise since only phase of the fundamental frequency is used to retrieve displacement. It has been demonstrated that even blurring and defocusing of optical images have little effect on the precision and accuracy of measurement results using this method[36,37] because blurring and defocusing act as low-pass filters hence only the higher order harmonics are degraded, leaving the fundamental frequency mostly untouched. This feature makes this method particularly suitable for dynamic displacement measurement since device is moving during exposure time of an image, leading to certain degree of blurring. One limitation of this displacement measurement method originates from the nature of high-speed camera that high frame rate must be compensated by reduced field of view. The small field of view at high frame rate has two consequences, one is that it can't include both sensors at the same time hence force in a specimen remains unknown which limits this optical method to be used in high strain rate testing where both stress and strain need to be obtained, the other is it rises the uncertainty in measured displacement as for the single frequency-based DFT method the less the repeated patterns are captured and used in the analysis the worse the measurement accuracy will be[35]. Another limitation of this method is that it is not suitable to measure displacement inside electron microscopes.

The other method is using a capacitive readout circuit to measure displacement since there is a linear relationship between displacement and capacitance difference in the sensors (Eq. 3). A commercially available capacitive readout AT1006 (ACT-LSI, Japan)[28] was used to convert the differential capacitance linearly into an output voltage. Figure 6a shows the function blocks of AT1006 and its connection to the MEMS chip, more specifically, channels X and Y are connected to Sensors A and B, respectively. Figure 6b shows an image of the

MEMS chip integrated with the readout. Before the readout can be used to measure displacement, calibration of the relationship between displacement and AT1006 output voltages change was conducted. The calibration result is linear as shown in Figure 7, in good agreement with Eq. 3. A NI DAQ (USB-6211 with the maximum sample rate of 250 kHz) was used to record the voltage reading from AT1006. Compared with the optical method, this method has two major advantages: 1) it can be used both in air and in vacuum, and 2) it can measure displacements of both sensors A and B at the same time with which force in a specimen can be calculated hence it can be used to in mechanical testing of nanowires. Unfortunately the bandwidth of this readout is relatively low (~1,100 Hz), to be reported later, which prevents this method from measuring high-frequency signals.

5. Results

5.1 Dynamic response under AC actuation force

To study dynamic response of the device under AC actuation force, AC actuation voltage with Vpp=30 V and different frequencies was applied to the actuator. Function generator Agilent 33250A was used to provide the voltage. Amplitude of the output displacement d_B was measured as a function of the actuation force frequency. Note that there is a factor of 2 between the actuation voltage frequency and the resulting actuation force (or displacement) frequency because of the square relationship as shown in Eq. 2.

Since only the electronic method can be used to measure displacement in vacuum but its relatively low bandwidth makes it unable to detect the resonance peaks as predicted in Section 3.1, measurements were focused on the dynamic response under AC actuation force in air using the optical method. For the optical method, in order to improve the measurement

accuracy, a larger field of view and more periodic beams are preferred, as discussed in Section 4.1. Hence to accurately measure displacement at high frequency, a low frame rate associated with large field of view was used. This way "aliasing" would occur hence the measured frequency is not the actual displacement oscillation frequency, but amplitude of the oscillation can still be retrieved correctly if the frame rate and exposure time are set properly. For example, a low frame rate of 100 fps with short exposure time can be used for displacement oscillation of 2,002 Hz (the actuation voltage frequency is purposely set as 1,001 Hz). In this case, an image is taken every 20.02 displacement oscillation cycles, these images record different phases of the oscillation waveform, from which the oscillation amplitude can be retrieved. Figure 8a shows the optically measured displacement of sensor B in this situation. As can be seen, although the measured frequency is not correct, the displacement amplitude was clearly recorded. The displacement amplitudes at different frequencies were then normalized by the amplitude at 1Hz. Figure 8b shows the measured relationship between the normalized displacement amplitude and the actuation frequency. Only the lower natural frequency in air was measured, which is 10.6 kHz, a little smaller than the counterpart in vacuum, 11.5 kHz, as calculated by the model in Section 3.1.

This measured relationship was then fitted using magnitude of normalized transfer function $\left|\frac{G(j2\pi f)}{G(j2\pi)}\right|$, where the denominator accounts for the normalization at 1 Hz. By fitting the curve in Figure 8, damping coefficients in air c_A= 3.09×10^{-4} kg/s and c_B= 2.83×10^{-4} kg/s were obtained. The damping coefficients can be used to calculate the second natural frequency f_4 and the device displacement in air under ramping actuation force in the next section. To summarize, f_1 to f_4 are 11.5, 70.2, 10.6, and 70.0 kHz, respectively.

5.2 Dynamic response under ramping actuation force: vacuum and air

In this section, the dynamic responses under ramping actuation force in both vacuum and air were first predicted. Then a ramping actuation force with gradually increasing loading velocity was applied to the device in both vacuum and air while Sensor B displacement was measured.

To provide a linear ramping actuation force, an actuation voltage profile $\mathrm{V}(t) = \lambda t^{0.5}$ was applied to the comb-drive actuator, where λ is a function of the loading rate ξ via Eq. 2. The larger λ, the smaller the time it takes to reach the desired actuation voltage (here the time is called the loading time). As an example, Figure 9 shows the actuation voltage profile up to 15 V with the loading time of 1 s. In this case $\lambda = 15\ \mathrm{V/s^{0.5}}$ in the actuation voltage profile, the loading rate $\xi = 24.2\ \mu\mathrm{N/s}$, and the loading velocity is 226 nm/s. Figures 10 and 11 show the displacement as a function of the loading time in both vacuum and air, as calculated by Eqs. 9 and 10, respectively. A series of testing was conducted, during which the actuation voltage was increased from 0 to 15 V while the loading time was gradually decreased to increase the loading velocity.

The vacuum experiments were conducted inside a SEM (FEI Quanta 3D FEG) chamber. Of course the vacuum was not absolute. The displacement d_B was measured using the capacitive readout and compared with the modeling result according to Eq. 9. Figure 10 shows the comparison when the loading velocity was 226 nm/s, 45.2 μm/s, and 226 μm/s (corresponding loading time of 1 s, 5 ms, and 1 ms). When the loading velocity was 226 nm/s (Figure 10a), the measured and modeled displacements agreed very well, both increasing linearly with time. When the loading velocity was increased to 45.2 μm/s (Figure 10b), the

electronically measured displacement started to show a small lag compared to the modelled displacement (about 2% smaller) due to the limitation in bandwidth. The sensor B velocity 45.2 μm/s in this case was thus considered to be the upper bound that can be measured using the capacitive readout AT1006. When the loading velocity was increased to 226 μm/s (Figure 10c), the electronic measurement was further lagged, again due to the limitation in bandwidth. The sinusoidal deviation appears to have only one frequency rather than two as predicted by Eq. 9. This is because the amplitude of the larger natural frequency is tiny compared that of the lower natural frequency. For example, when the loading velocity is 226 μm/s, the calculated amplitude is 3.2 nm for the lower natural frequency, while 0.01 nm for the larger natural frequency. Of note is that even the lower natural frequency predicted is 11,490 Hz, much larger than the capacitive readout bandwidth.

The dynamic response under the ramping actuation force was also studied in air. The optical method was used to measure the displacement d_B. Figure 11a to c shows the experimentally measured and analytically predicted displacement d_B with the loading velocity of 226 nm/s, 226 μm/s, and 2.26 mm/s. The corresponding loading time was 1 s, 1 ms, and 0.1 ms. The high-speed camera frame rate used was 50, 16,000, and 95,000 fps with the corresponding images under these frame rates shown in Figure 11e to f, respectively. As mentioned earlier, the field of view was reduced to compensate the increasing frame rate. The measured displacement agreed well with analytical model. As shown in Figure 11b, optically measured displacement increased with time with no obvious lag when the loading velocity was 226 μm/s, which also proved that the significant lag in Figure 10c is due to the bandwidth limitation of the electronic measurement. When the loading speed increased to

2.26 mm/s, measured displacement can still reasonably match the model prediction. However, the displacement exhibited large nonlinearity, as discussed in Section 3.2, which could be challenging for high-rate testing with a constant strain rate.

6. Discussion

6.1 Loading velocity and strain rate

In this section, the maximum loading velocity and strain rate attainable by the present device are discussed. For this microscopic tensile testing device, it can be seen from Eqs. 9 and 10 that under a ramping actuation force, the strain rate will not be a constant either in vacuum or in air because displacement of Sensor B is not absolutely linear. Generally speaking, high strain-rate testing does not necessarily require an absolute constant strain rate, which is indeed very difficult to achieve if possible at all. For example, commercial macroscopic high-rate testing systems can use servohydraulic actuators to reach strain rate up to 500 s^{-1}, beyond which dynamic testing techniques such as Hopkinson bar technique are used. Open-loop control is used since the actuator moves at such a high velocity that real-time close-loop control is not as effective, which leads to displacement that cannot be absolutely linear[43-45]. Therefore it is reasonable to carry out high-rate testing with approximately constant strain rate.

For a given loading velocity, the strain rate would depend on the specimen length. Hence for the generality of the conclusions, loading velocity will be discussed followed with strain rate. To perform a constant-strain-rate test, two requirements should be met: (1) displacement measurement is sufficiently fast such that measured displacement is accurate, and (2) displacement must be linear with time with negligible deviation. The first requirement has

been addressed in the preceding section, which resulted in the maximum loading velocities of 45.2 μm/s and 2.26 mm/s using the capacitive readout and optical measurement, respectively, with the corresponding maximum strain rates of 22.6 s^{-1} and 1130 s^{-1} (assuming the specimen length of 2 μm).

Now let us assess the second requirement. To do so, a normalized term "deviation ratio" is defined as the maximum displacement deviation during the loading divided by the travel range. Since the first requirement has been satisfied, the maximum displacement deviation here will be discussed based on theoretical result. The deviation ratio apparently depends on the travel range (i.e., maximum displacement). For the present device, two travel ranges, 60 and 200 nm, are selected for the purpose of discussion (corresponding to 3% and 10% strain for a typical nanowire sample with gauge length of 2 μm). For the capacitive readout with the loading velocity of 45.2 μm/s (Figure 10b), the deviation ratio is less than 1% for both travel ranges. For the optical measurement with the loading velocity of 2.26 mm/s (Figure 11c), the deviation ratio is 50% and 15%, respectively. On the other hand, for a given allowable deviation ratio, the maximum displacement deviation can be determined, from which the maximum loading rate ξ_{max} and hence the maximum loading velocity and strain rate are obtained. For example, in air, with 10% allowable deviation ratio, the maximum loading velocity is 416 μm/s and 1.39 mm/s for the travel range of 60 and 200 nm, respectively, with the corresponding maximum strain rates of 208 s^{-1} and 693 s^{-1}.

Note that the deviation ratio here is defined based on the deviation from the linear displacement in theory (i.e. $\frac{\xi t}{k_{SB}}$ in Eq. 9), which is an overestimate if compared with a fitting line that would also give a constant strain rate. Another way to evaluate how linear the

displacement curve is, a straight linear is used to fit the curve and the coefficient of determination (R^2) is obtained. The R^2 values for linear fitting of two displacement ranges (60 and 200 nm) in both vacuum and air are all over 97%, indicating reasonably good linear fitting. In summary, it is appropriate to conclude that the attainable strain rate is 22.6 s^{-1} and on the order of 200 s^{-1} using the capacitive readout and optical measurement, respectively.

Of note is that the electrostatic actuator can deliver fast actuation and hence high strain rate regardless of the environment (air or vacuum). As mentioned, the bandwidth of a thermal actuator is determined by the heat transfer characteristic of the heater (i.e., heating rate and heat dissipation rate). The bandwidth depends on the environment (air or vacuum) as the heat dissipation is related to the environment. More specifically, in air the bandwidth is higher because of the effective heat dissipation to the substrate through air (if there is a substrate immediately below the device [38]). By contrast, in vacuum the heat only dissipates through the anchors at the two ends [39].

In addition, the loading velocity and strain rate discussed so far are for the case of no specimen mounted on the device. When a specimen is mounted, the loading velocity and strain rate will decrease. The larger the stiffness of the specimen relative to the stiffness of the device, the more the decrease will be.

6.2 Damping coefficients

For this device, the damping force comes from the comb-drive actuator and parallel plates sensors. For the comb-drive actuator, a laterally driven structure, viscous drag of ambient fluid is the dominant damping source; while for the parallel plates sensor, squeeze film damping is the major source of energy dissipation[40]. Both damping mechanisms have

been studied extensively and here we will briefly discuss them in the context of our device.

Damping coefficient for a comb-drive actuator can be expressed as[41]

$$c_{cd} = \mu\left(\frac{A_{eff}}{d_s} + \frac{A_{eff}}{\delta} + \frac{A_s}{g} + 10.7L\right) \quad (11)$$

where μ is the viscosity of air, A_{eff} is the effective plate area including the areas of the shuttle, fingers and beams, A_s is the side area of the actuator, d_s is the distance between the actuator and substrate, δ is the effective decay distance, and L is the characteristic dimension of the moving structure that can be taken as half the width of the shuttle.

the squeeze film damping force on parallel plates can be either elastic force proportional to displacement of the moving plate at a high frequency or viscous force proportional to velocity of the moving plate at a low frequency[42]. The cutoff frequency or frequency at which the two kinds of damping force are equal can be expressed as[42]

$$\omega_c = \frac{\pi^2 g_1^2 p_a}{12\mu w^2} \quad (12)$$

where p_a is the atmosphere pressure and w is the width of the plate. For the device reported here, this cutoff frequency is calculated to be 3.7 MHz. Since the device is operated far below this frequency, the viscous damping force dominates while elastic damping force is negligible. In this situation, the damping coefficient for parallel plates can be expressed as[42]

$$c_{pp} = \frac{\mu L w^3}{g_1^3} \quad (13)$$

where L is length of the plate.

Based on these theoretical models, the calculated damping coefficients in air are c_A= 3.04×10^{-4} kg/s (comb-drive actuator and parallel-plate sensor A) and c_B= 2.98×10^{-4} kg/s (parallel-plate sensor B), close to the experimentally obtained values in Section 5.1.

6.3 Force measurement

The capacitive readout AT1006 is used to obtain force and elongation of a specimen on the present device because it is able to measure both sensors' displacements in SEM at the same time. As mentioned in Section 2, when the device is operated for quasi-static testing, force on the specimen equals the force in the load cell, which can be calculated given displacements of the two sensors. For high strain rate dynamic testing, force on the specimen equals the force in the load cell minus the damping force and the inertia force of the proof mass. Eq. 5 can be rewritten as

$$F_S = k_S d_B = k_{LC}(d_A - d_B) - c_B \dot{d}_B - m_B \ddot{d}_B \quad (14)$$

where the first subtracted term is the damping force and the second the inertia force.

The damping force inside SEM environment with a pressure of 5×10^{-6} torr was hence studied. In rarefied air, the squeeze film air damping coefficient can be calculated using Veijola's model[46] that replaces the viscosity in Eq. 13 with an "effective" one μ_{eff},

$$\mu_{eff} = \frac{\mu}{1+9.658K_n^{1.159}} \quad (15)$$

where K_n is Knudsen number that is defined as mean free path of air molecules divided by gap distance of the parallel plate. The damping coefficient calculated in this case is on the order of 10^{-12} Kg/s. The damping force is on the order of 10^{-15} N, even for the largest velocity (45.2 $\mu m/s$) that can be measured by AT1006. Therefore the damping force inside SEM is negligible and force of a specimen can still be calculated based on the load cell force.

In air, the damping coefficient is on the order of 10^{-4} Kg/s. With a strain rate of 208 s^{-1}, the damping force is about 40 nN, which can still be neglected for testing specimens like nanowires.

For the inertia force, we only consider it in the vacuum as the upper bound. The acceleration is given by

$$\ddot{d}_B = a_1\xi\ (2\pi f_1)^2 sin(2\pi f_1 t) - a_2\xi\ (2\pi f_2)^2 sin(2\pi f_2 t) \quad (16)$$

a_1 and a_2 were calculated to be $118.6 \times 10^{-9}\ and\ 0.52 \times 10^{-9}\ m \cdot s/N$ with the known system parameters (*e.g.*, m_A, m_B, k_{SB}, k_{LC}). Even for the maximum loading rate $\xi = 44.0\ mN/s$ (corresponding to the maximum loading velocity is 416 μm/s and strain rate of 208/s), the maximum acceleration is 31.6 m/s^2, and the maximum inertia force is 0.19 μN (with the mass m_B = 5.99×10^{-9} kg), which is well below 1% of the force to break a typical nanowire. Moreover, the inertia force oscillates following a sinusoidal form, so it at most adds to the noise level without causing a systematic error.

7. High-Strain-Rate Testing of Gold Nanowires

To demonstrate of its capability of high strain-rate nanomechanical tensile testing, the device was used to test two single-crystalline gold nanowires at strain rates of 10^{-5} s^{-1} and 10 s^{-1}. The gold nanowires, <110> oriented, were synthesized by physical vapor deposition exhibiting high crystalline quality[47]. The tests were conducted inside SEM and AT1006 was used to measure displacements of the two sensors (A and B), from which the stress and strain were calculated. Nanowires were picked up from a Si substrate using a nanomanipulator (Klocke Nanotechnik, Germany) and clamped on the device by e-beam induced deposition of Pt[24,8]. The diameters of the two nanowires were 144 nm and 153 nm, respectively. Both the nanomanipulation and the tensile testing were performed inside a SEM-FIB dual beam (FEI Quanta 3D FEG).

Stress-strain curves for the two tested nanowires are shown in Figure 12a. Young's

moduli measured from both tests are around 75 GPa, which is close to the bulk value. The gold nanowire tested at 10^{-5} s^{-1} exhibited a fracture strength of 2.1 GPa and a fracture strain of 2.8 %, indicating a brittle fracture. By contrast, the one tested at 10 s^{-1} showed a higher yield strength of 3.7 GPa and a large ductility with the fracture strain of 13.5 %. Note a sudden stress drop was also captured during high-speed loading of the nanowire. This softening behavior is attributed to the nucleation and propagation of leading partial dislocations from the nanowire surface, which has been reported in previous work on FCC metal nanowires[15,48-49]. The stress-time and strain-time curves are also shown (Figure 12b and c). It can be seen that the strain rate was constant until the softening took place. During the softening process, the specimen strain rate increased even though the applied electrostatic load still increased at a constant rate, because the specimen stiffness decreased. The strain rate of 10 s^{-1} was before the softening.

Figure 13 shows the two nanowires before and after testing. By comparing the SEM images, we found that the nanowire tested at high strain rate shows a clear decrease in diameter across the gage length while the one tested at low strain rate did not show much variation in diameter. It is well known that for metal nanowires plastic deformation starts with surface dislocation nucleation. When two dislocations glide on nonparallel planes inside the crystal, they can form sessile dislocations leading to strain hardening and delayed necking. This feature is more prominent as the strain rate increases and the dislocation density increases, which explains why a more uniform decrease in diameter occurs under high strain rates; by contrast, necking occurs at lower strain rates. This observation is similar to the results by Ramachandramoorthy[19] and Tao[50].

8. Conclusions

In this paper, we systematically investigated the dynamic response a MEMS-based nanomechanical testing device in air and in vacuum. The MEMS device consists of an electrostatic actuator, a load cell and two capacitive displacement sensors. A dynamic model of the device was built and displacement of sensor B under AC actuation force and ramping actuation force in both air and vacuum were simulated. Both capacitive readout and high-speed optical imaging were used to measure the displacements. The experimental results showed good agreement with the modeling results. The maximum strain rate the device can attain was found to be about 200 s^{-1}. However, the capacitive readout used can only measure strain rate up to 22.6 s^{-1} (gauge length 2 μm) due to its limited bandwidth, which is nevertheless an order of magnitude higher than the highest strain rate (2 s^{-1}) reported so far using an electronic sensor. We demonstrated the device's capability by testing single-crystalline gold nanowires at two strain rates of 10^{-5} s^{-1} and 10 s^{-1}. It was found that increasing strain rate leads to higher yield strength and larger ductility.

8. Acknowledgement

The authors gratefully acknowledge financial support from the National Science Foundation (NSF) through Award Nos. DMR-1410475 and CMMI-1762511. The authors would like to thank Dr. G. Richter for providing the Au nanowires.

Appendix

Dynamic response of a single-mass-spring system under ramping force

For a single-mass-spring system as schematically shown in Figure A1, if the input force is a ramping force $F(t) = pt$, the equation of motion can be written as

$$m\ddot{x} + kx = pt \tag{A1}$$

Solution to this equation is $x(t) = \frac{pt}{k} - \frac{p}{k}\sqrt{\frac{m}{k}}sin\left(\sqrt{\frac{k}{m}}t\right)$. This solution contains two terms; the first is a ramping term $\frac{pt}{k} = \frac{F(t)}{k}$, and the second is a sinusoidal term $-\frac{p}{k}\sqrt{\frac{m}{k}}sin\left(\sqrt{\frac{k}{m}}t\right)$. The sinusoidal term has a frequency $\sqrt{\frac{k}{m}}$, which is the natural frequency of the system. Its amplitude is proportional to loading rate p and can be calculated if system parameters m and k are known.

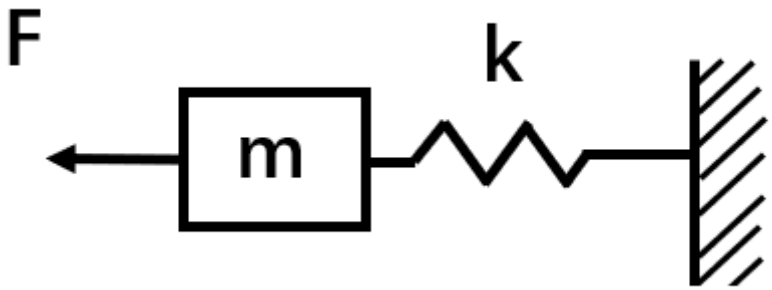

Fig. A1. Schematic of a single-mass-spring system.

Dynamic response of a single-mass-spring-damper system under ramping force

For a single-mass-spring-damper system as schematically shown in Figure A2, if the input force is a ramping force $F(t) = pt$, the equation of motion can be written as

$$m\ddot{x} + c\dot{x} + kx = pt \tag{A2}$$

If the system is an underdamped system, solution to this equation is $x(t) = \frac{pt}{k} - \frac{cp}{k^2} -$

$\frac{2pm}{k\sqrt{4mk-c^2}}\sin\left(\frac{\sqrt{4mk-c^2}}{2m}t+\theta\right)$, where $\theta=\arctan\left(\frac{c\sqrt{4mk-c^2}}{c^2-2km}\right)$. The solution contains three terms; the first is a ramping term $\frac{pt}{k}=\frac{F(t)}{k}$, the second is a constant $-\frac{cp}{k^2}$, and the third is a sinusoidal term $-\frac{2pm}{k\sqrt{4mk-c^2}}\sin\left(\frac{\sqrt{4mk-c^2}}{2m}t+\theta\right)$. The sinusoidal term has a frequency $\frac{\sqrt{4mk-c^2}}{2m}$, which is the damped natural frequency of the system.

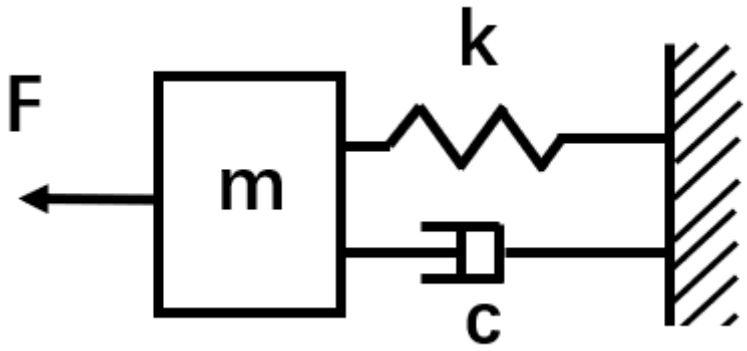

Fig. A2. Schematic of a single-mass-spring-damper system.

Reference:

1. Yao S, Zhu Y (2015) Nanomaterial‐enabled stretchable conductors: strategies, materials and devices. Advanced materials 27 (9):1480-1511
2. Yao S, Swetha P, Zhu Y (2018) Nanomaterial‐Enabled Wearable Sensors for Healthcare. Advanced healthcare materials 7 (1):1700889
3. Gong S, Cheng W (2017) One‐Dimensional Nanomaterials for Soft Electronics. Advanced Electronic Materials 3 (3):1600314
4. Zhu Y, Ke C, Espinosa H (2007) Experimental techniques for the mechanical characterization of one-dimensional nanostructures. Experimental Mechanics 47 (1):7
5. Park HS, Cai W, Espinosa HD, Huang H (2009) Mechanics of crystalline nanowires. MRS bulletin 34 (3):178-183
6. Zhu Y (2017) Mechanics of Crystalline Nanowires: An Experimental Perspective. Applied Mechanics Reviews 69 (1):010802
7. Zhu T, Li J, Ogata S, Yip S (2009) Mechanics of ultra-strength materials. Mrs Bulletin 34 (3):167-172
8. Cheng G, Chang T-H, Qin Q, Huang H, Zhu Y (2014) Mechanical properties of silicon carbide nanowires: effect of size-dependent defect density. Nano letters 14 (2):754-758
9. Richter G, Hillerich K, Gianola DS, Monig R, Kraft O, Volkert CA (2009) Ultrahigh strength single crystalline nanowhiskers grown by physical vapor deposition. Nano Letters 9 (8):3048-3052

10. Xu F, Qin Q, Mishra A, Gu Y, Zhu Y (2010) Mechanical properties of ZnO nanowires under different loading modes. Nano Research 3 (4):271-280
11. Agrawal R, Peng B, Gdoutos EE, Espinosa HD (2008) Elasticity size effects in ZnO nanowires− a combined experimental-computational approach. Nano letters 8 (11):3668-3674
12. Zhu Y, Qin Q, Xu F, Fan F, Ding Y, Zhang T, Wiley BJ, Wang ZL (2012) Size effects on elasticity, yielding, and fracture of silver nanowires: In situ experiments. Physical review B 85 (4):045443
13. Zhu T, Li J, Samanta A, Leach A, Gall K (2008) Temperature and strain-rate dependence of surface dislocation nucleation. Physical Review Letters 100:025502
14. Chen LY, He M-r, Shin J, Richter G, Gianola DS (2015) Measuring surface dislocation nucleation in defect-scarce nanostructures. Nature materials 14 (7):707
15. Qin Q, Yin S, Cheng G, Li X, Chang T-H, Richter G, Zhu Y, Gao H (2015) Recoverable plasticity in penta-twinned metallic nanowires governed by dislocation nucleation and retraction. Nature communications 6:5983
16. Zhong L, Sansoz F, He Y, Wang C, Zhang Z, Mao SX (2017) Slip-activated surface creep with room-temperature super-elongation in metallic nanocrystals. Nature materials 16 (4):439
17. Bernal RA, Aghaei A, Lee S, Ryu S, Sohn K, Huang J, Cai W, Espinosa H (2014) Intrinsic Bauschinger effect and recoverable plasticity in pentatwinned silver nanowires tested in tension. Nano letters 15 (1):139-146
18. Chang T-H, Zhu Y (2013) A microelectromechanical system for thermomechanical testing of nanostructures. Applied Physics Letters 103 (26):263114
19. Ramachandramoorthy R, Gao W, Bernal R, Espinosa H (2015) High strain rate tensile testing of silver nanowires: rate-dependent brittle-to-ductile transition. Nano letters 16 (1):255-263
20. Cheng G, Miao C, Qin Q, Li J, Xu F, Haftbaradaran H, Dickey EC, Gao H, Zhu Y (2015) Large anelasticity and associated energy dissipation in single-crystalline nanowires. Nature nanotechnology 10 (8):687
21. Peng C, Zhong Y, Lu Y, Narayanan S, Zhu T, Lou J (2013) Strain rate dependent mechanical properties in single crystal nickel nanowires. Applied Physics Letters 102 (8):083102
22. Zhu Y, Chang T-H (2015) A review of microelectromechanical systems for nanoscale mechanical characterization. Journal of Micromechanics and Microengineering 25 (9):093001
23. Haque M, Saif M (2002) In-situ tensile testing of nano-scale specimens in SEM and TEM. Experimental mechanics 42 (1):123-128
24. Zhu Y, Espinosa HD (2005) An electromechanical material testing system for in situ electron microscopy and applications. Proceedings of the National Academy of Sciences 102 (41):14503-14508
25. Kang W, Saif MTA (2011) A novel SiC MEMS apparatus for in situ uniaxial testing of micro/nanomaterials at high temperature. Journal of Micromechanics and Microengineering 21 (10):105017
26. Naraghi M, Kolluru PV, Chasiotis I (2014) Time and strain rate dependent mechanical behavior of individual polymeric nanofibers. Journal of the Mechanics and Physics of Solids 62:257-275

27. Naraghi M, Chasiotis I, Kahn H, Wen Y, Dzenis Y (2007) Novel method for mechanical characterization of polymeric nanofibers. Review of scientific instruments 78 (8):085108
28. Tsuchiya T, Ura Y, Sugano K, Tabata O (2012) Electrostatic Tensile Testing Device With Nanonewton and Nanometer Resolution and Its Application to C_{60} Nanowire Testing. Journal of Microelectromechanical Systems 21 (3):523-529
29. Zhu Y, Corigliano A, Espinosa HD (2006) A thermal actuator for nanoscale in situ microscopy testing: design and characterization. Journal of Micromechanics and Microengineering 16 (2):242
30. Guan C, Zhu Y (2010) An electrothermal microactuator with Z-shaped beams. Journal of Micromechanics and Microengineering 20 (8):085014
31. Naraghi M, Chasiotis I (2009) Optimization of comb-driven devices for mechanical testing of polymeric nanofibers subjected to large deformations. Journal of Microelectromechanical Systems 18 (5):1032-1046
32. Zhu Y, Moldovan N, Espinosa HD (2005) A microelectromechanical load sensor for in situ electron and x-ray microscopy tensile testing of nanostructures. Applied physics letters 86 (1):013506
33. Pantano MF, Bernal RA, Pagnotta L, Espinosa HD (2015) Multiphysics design and implementation of a microsystem for displacement-controlled tensile testing of nanomaterials. Meccanica 50 (2):549-560
34. Erismis MA (2013) Design and modeling of a new robust multi-mass coupled-resonator family with dynamic motion amplification. Microsystem Technologies 19(8):1105-1110.
35. Yamahata C, Sarajlic E, Krijnen GJ, Gijs MA (2010) Subnanometer translation of microelectromechanical systems measured by discrete Fourier analysis of CCD images. Journal of Microelectromechanical Systems 19 (5):1273-1275
36. King H, Warnat S, Hubbard T Effect of image degradation on nm-scale MEMS FFT optical displacement measurements. In: Electrical and Computer Engineering (CCECE), 2015 IEEE 28th Canadian Conference on, 2015. IEEE, pp 1387-1392
37. Ellerington N, Bschaden B, Hubbard T, Kujath M (2012) Fourier analysis of blurred images for the measurement of the in-plane dynamics of MEMS. Journal of Micromechanics and Microengineering 22 (3):035019
38. Shroff SS., Boer MP（2015）Constant Velocity High Force Microactuator for Stick-Slip Testing of Micromachined Interfaces. Journal of Microelectromechanical Systems 24(6):1868-1877.
39. Lott CD, McLain TW, Harb JN, Howell LL (2002) Modeling the thermal behavior of a surface-micromachined linear-displacement thermomechanical microactuator. Sensors and Actuators A: Physical 101(1-2):239-250.
40. Zhang X, Tang WC Viscous air damping in laterally driven microresonators. In: Micro Electro Mechanical Systems, 1994, MEMS'94, Proceedings, IEEE Workshop on, 1994. IEEE, pp 199-204
41. Bao M (2005) Analysis and design principles of MEMS devices. Elsevier,
42. Bao M, Yang H (2007) Squeeze film air damping in MEMS. Sensors and Actuators A: Physical 136 (1):3-27
43. Boyce BL, Crenshaw TB (2005) Servohydraulic methods for mechanical testing in the sub-Hopkinson rate regime up to strain rates of 500 1/s. Sandia National Laboratories

Report:1-16
44. Zhu D, Rajan S, Mobasher B, Peled A, Mignolet M (2011) Modal analysis of a servo-hydraulic high speed machine and its application to dynamic tensile testing at an intermediate strain rate. Experimental Mechanics 51 (8):1347-1363
45. de Andrade Silva F, Zhu D, Mobasher B, Soranakom C, Toledo Filho RD (2010) High speed tensile behavior of sisal fiber cement composites. Materials Science and Engineering: A 527 (3):544-552
46. Veijola T, Kuisma H, Lahdenperä J, Ryhänen T (1995) Equivalent-circuit model of the squeezed gas film in a silicon accelerometer. Sensors and Actuators A: Physical 48 (3):239-248
47. Sedlmayr A, Bitzek E, Gianola DS, Richter G, Mönig R, Kraft O (2012) Existence of two twinning-mediated plastic deformation modes in Au nanowhiskers. Acta Materialia 60 (9):3985-3993
48. Park HS, Zimmerman JA (2005) Modeling inelasticity and failure in gold nanowires. Physical Review B 72 (5):054106
49. Cheng G, Yin S, Chang T, Richter G, Gao H, Zhu Y (2017) Anomalous Tensile Detwinning in Twinned Nanowires. Physical Review Letters 119(25):256101.
50. Tao W, Cao P, Park HS (2018) Atomistic simulation of the rate-dependent ductile-to-brittle failure transition in bicrystalline metal nanowires. Nano letters 18 (2):1296-1304

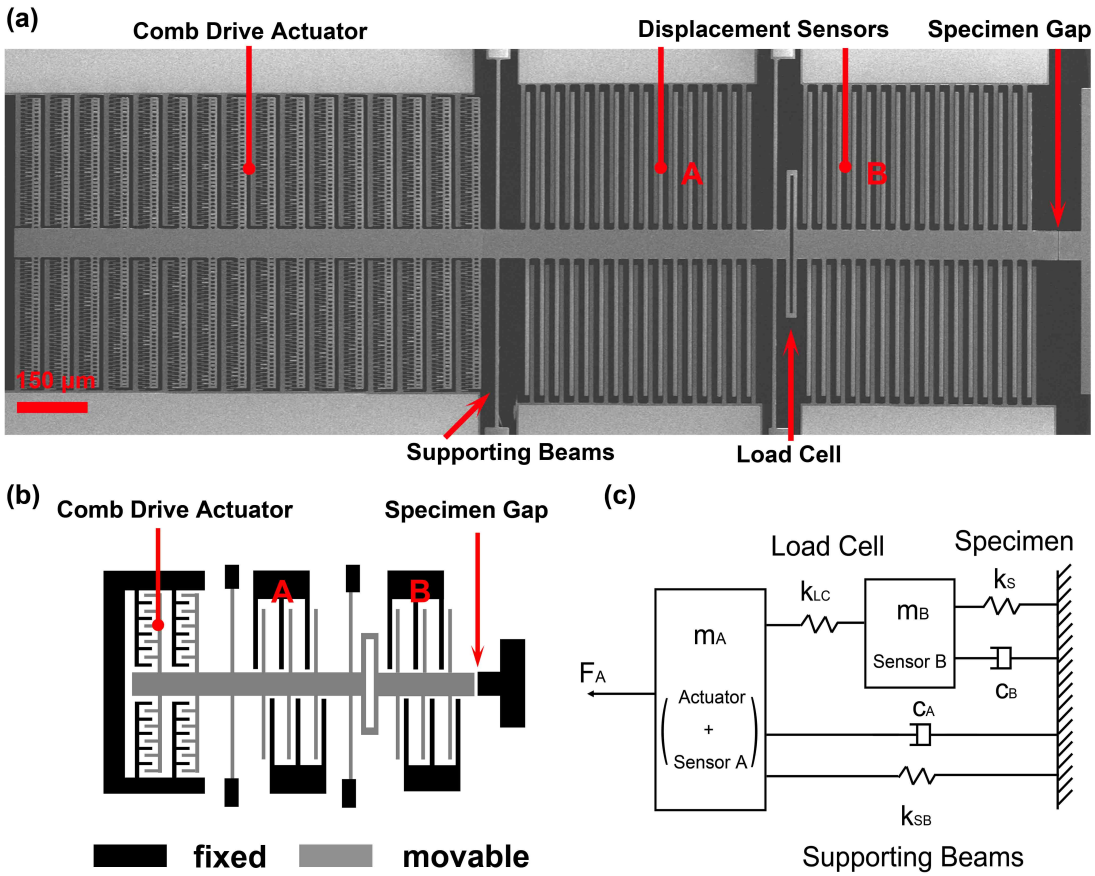

Fig. 1. (a) SEM micrograph of the fabricated device. (b) Schematic of MEMS device configuration. (c) Device lumped mechanical model.

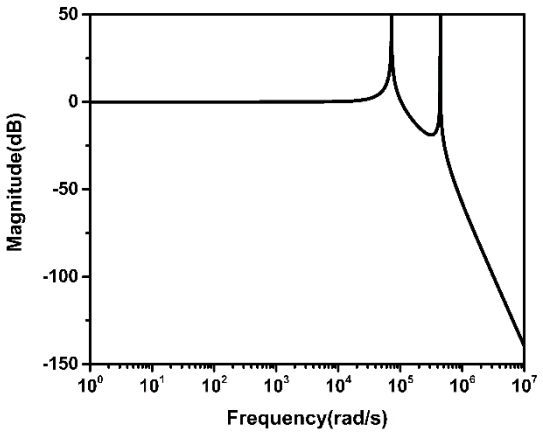

Fig. 2. Bode magnitude plot of the device in vacuum.

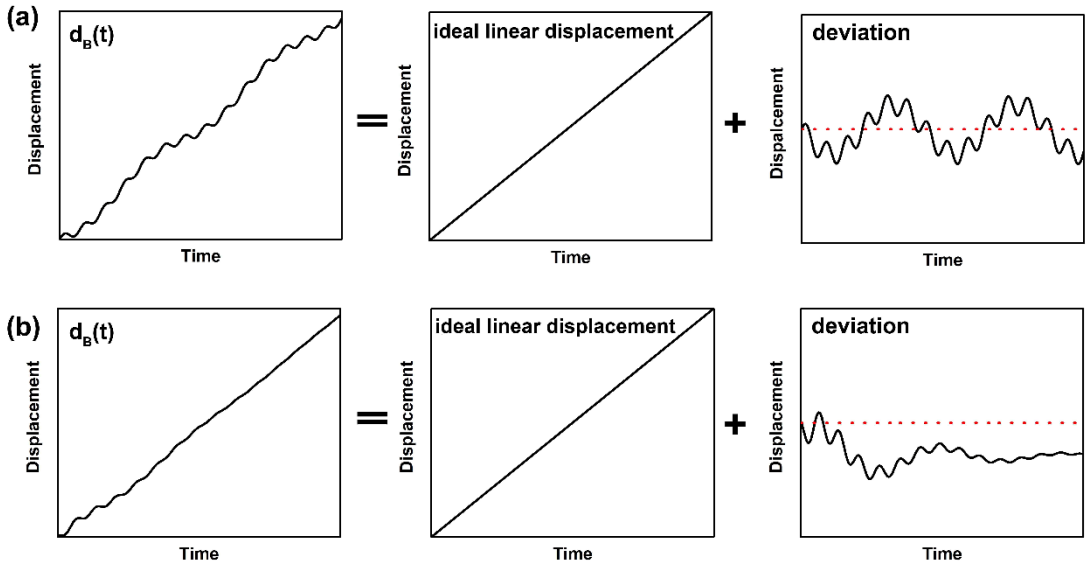

Fig. 3. Illustration of Sensor B displacement when the device is actuated by a linear ramping force (a) in vacuum, (b) in air. For both cases, Sensor B displacement is the superposition of an ideal linear displacement (constant velocity and correspondingly constant strain rate) and deviation. Horizontal dashed line marks zero deviation.

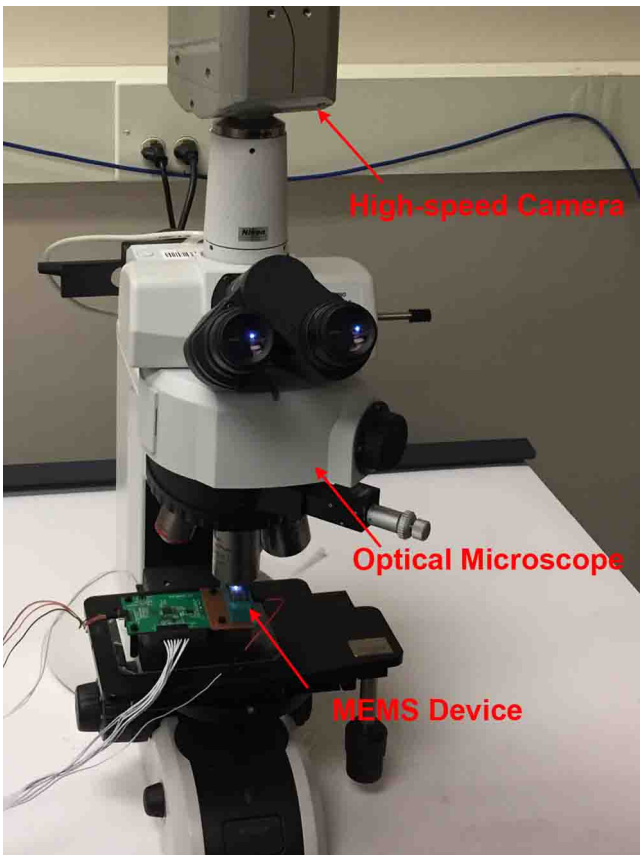

Fig. 4. Experiment setup to measure the displacement including a high-speed camera and an optical microscope.

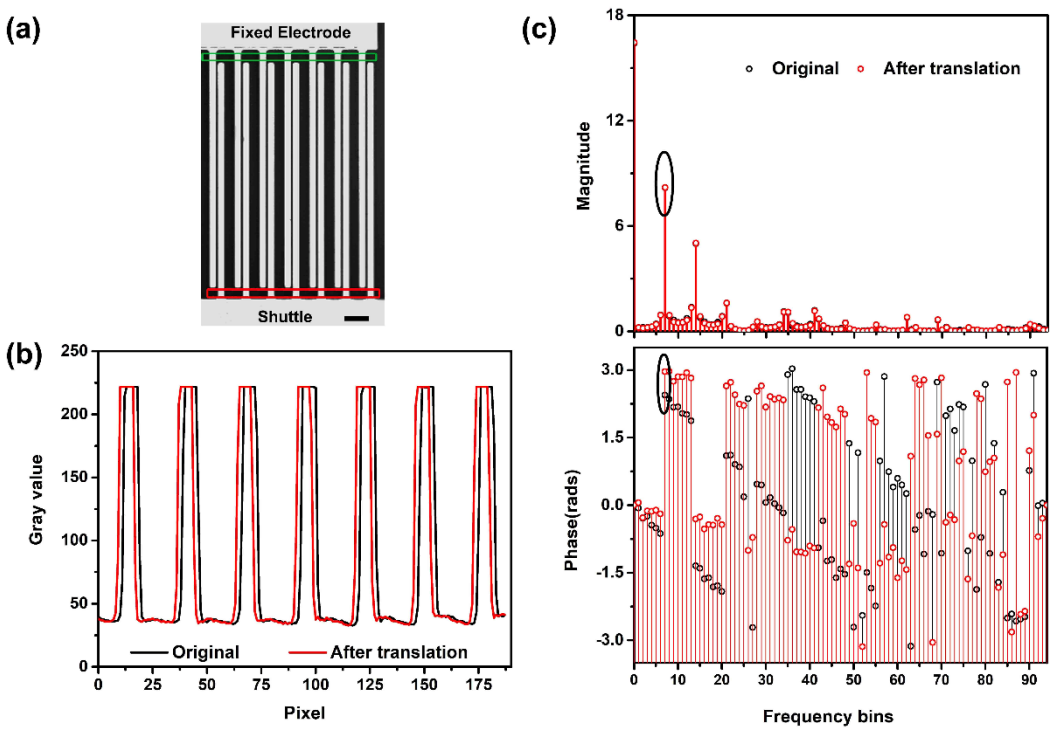

Fig. 5. (a) One frame of the high-speed image. Scale bar 30 μm. (b) 1D line intensity profile of the periodic pattern in the region of interest before and after translation. (c) DFT of the line intensity profile before and after translation (upper is magnitude plot and lower is phase plot). Fundamental frequency corresponding to the spatial frequency of the periodic patterns is circled out. Phase shift of the fundamental frequency is used to retrieve the translational displacement.

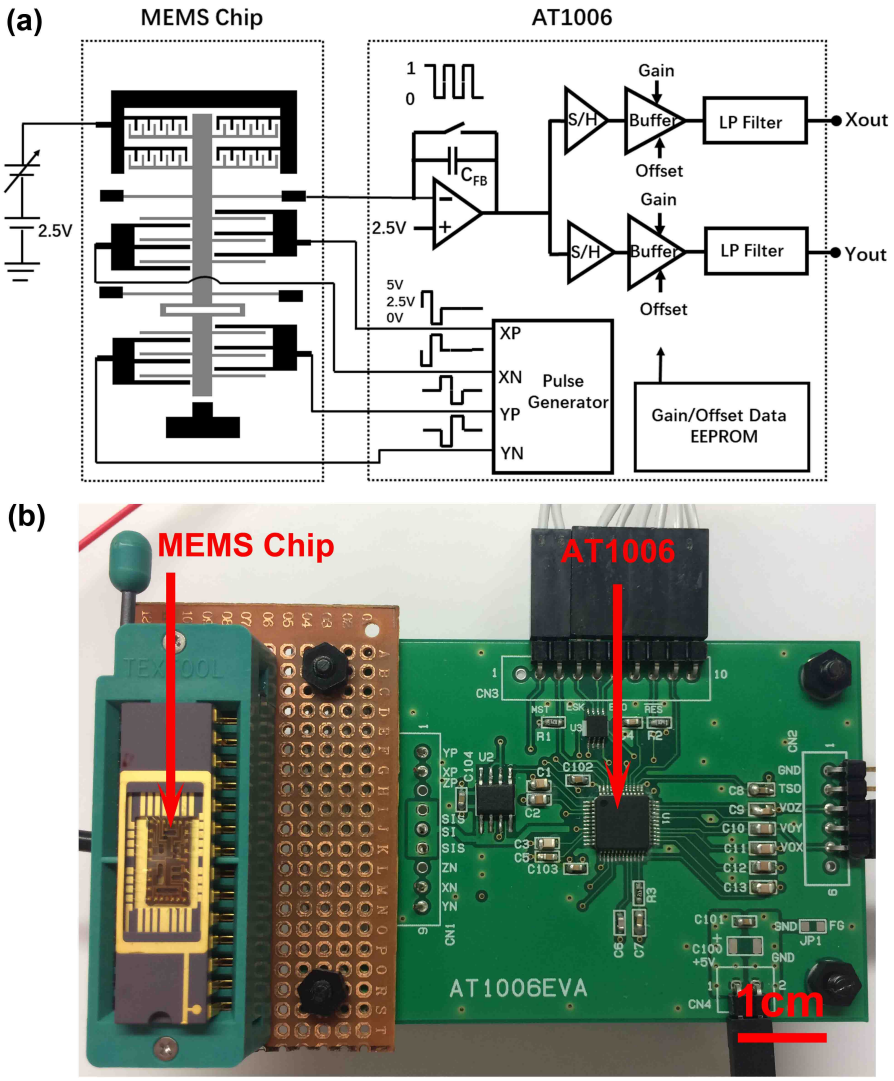

Fig. 6. (a) Functional block diagram of the capacitive readout AT1006 and its connection with the MEMS device. (b) Image of the MEMS device and the capacitive readout.

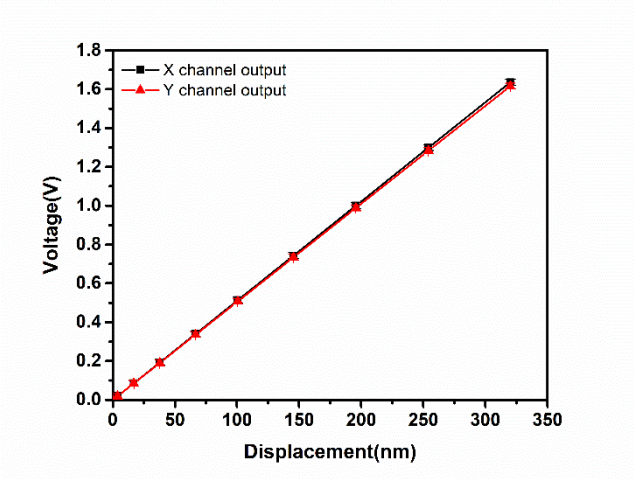

Fig. **7**. Calibrated relationship between AT1006 output voltages and measured displacements of sensor A and B.

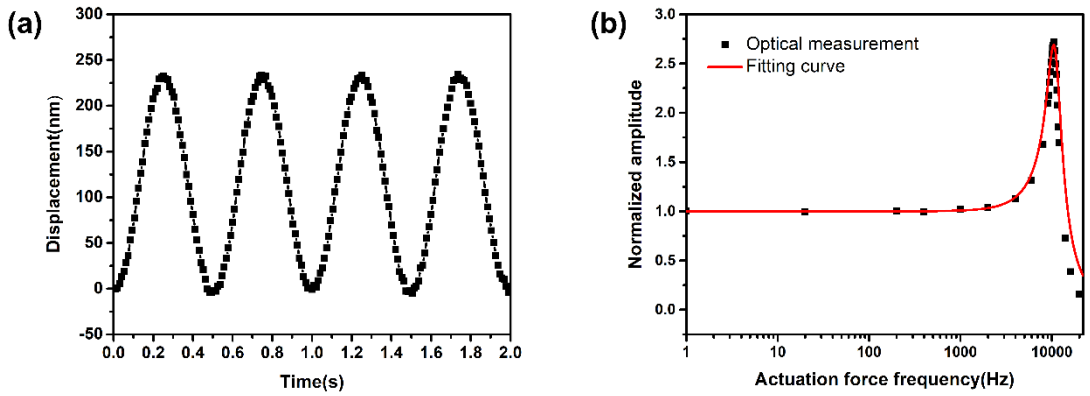

Fig. 8. (a) Optically measured displacement at frequency of 2002 Hz (the frame rate used is 100 fps). (b) Relationship between actuation force frequency and normalized displacement amplitude measured using the optical method. The optical measurement result was fitted, from which the damping coefficients in air were obtained.

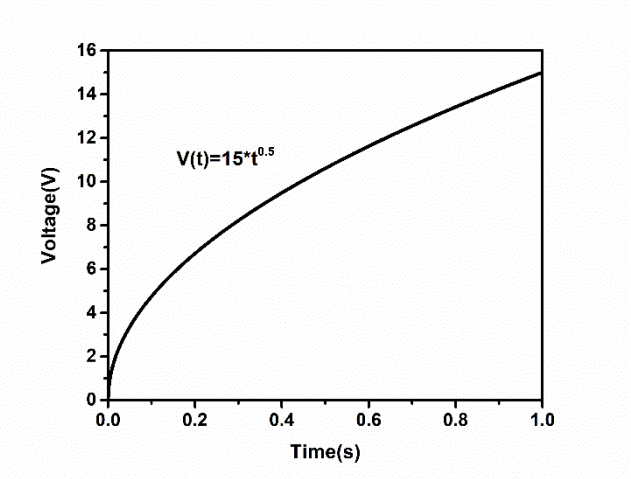

Fig. 9. Voltage profile to achieve the linearly ramping actuation force (loading time of 1 s).

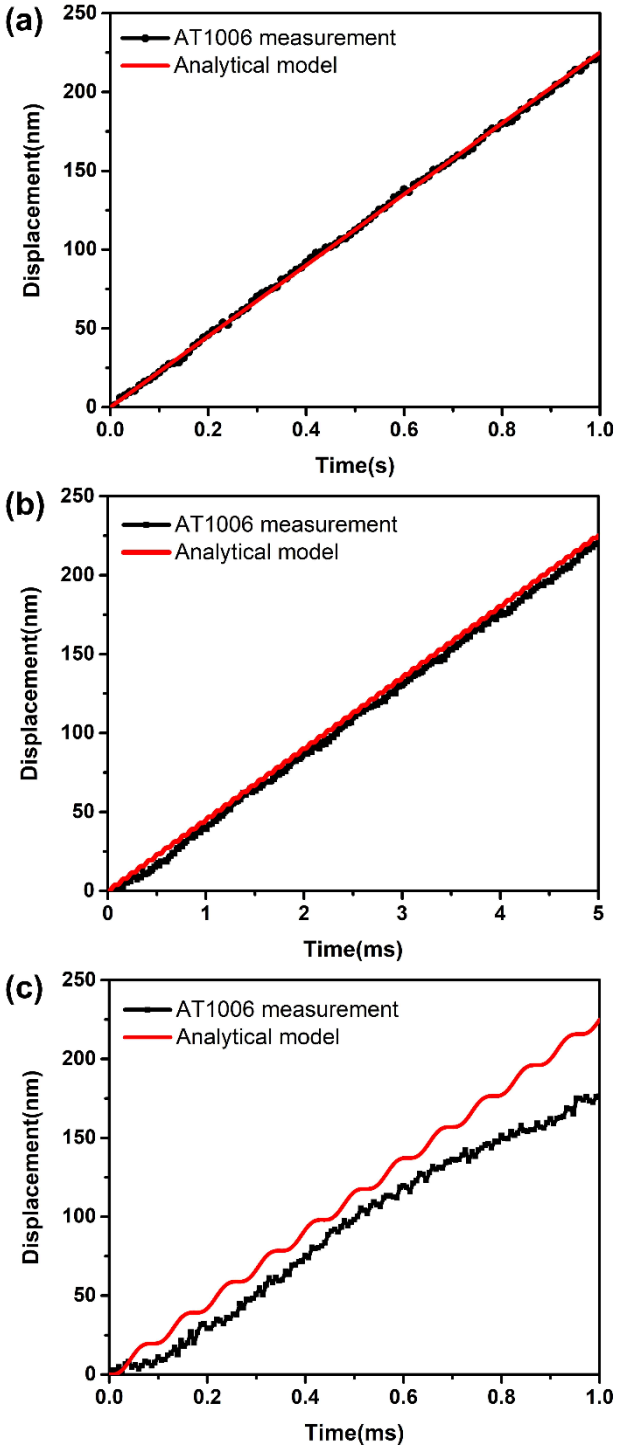

Fig. 10. Comparison of displacements from the dynamics and measured using AT1006 in vacuum when loading time is (a) 1 s, (b) 5 ms, and (c) 1 ms.

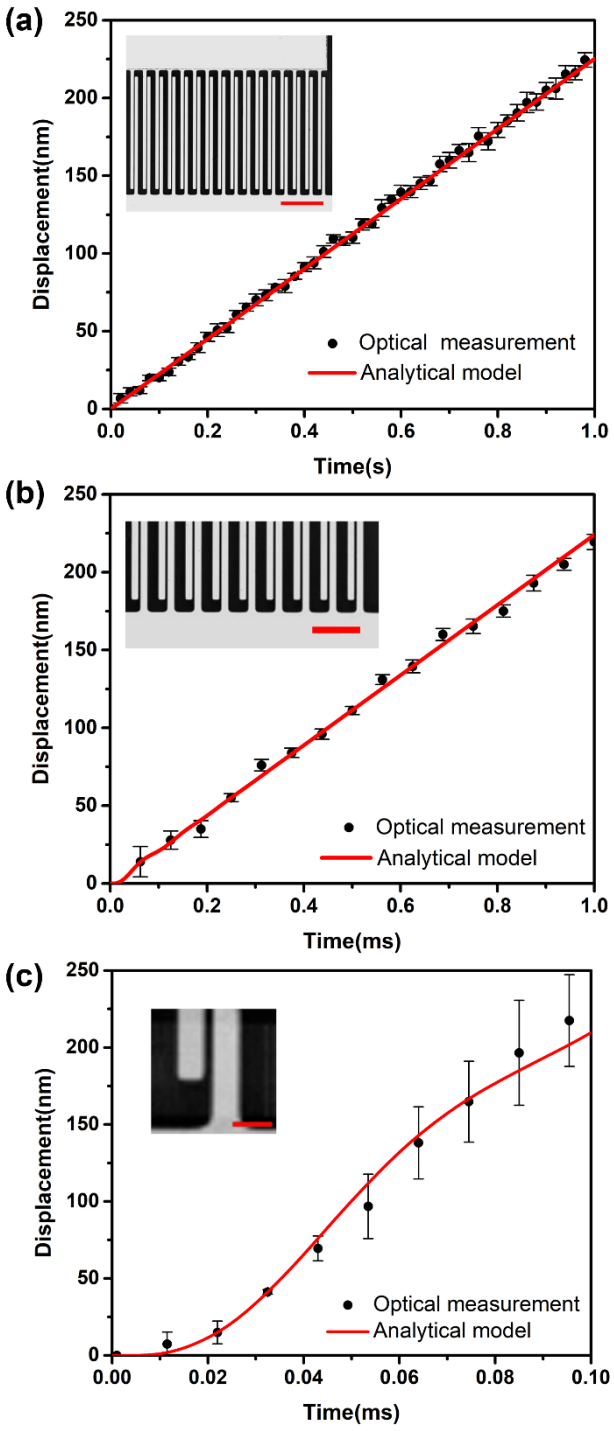

Fig. 11. Comparison of displacements from the dynamics model and measured optically in air when loading time is (a) 1 s, (b) 1 ms, and (c) 0.1 ms. The frame rates are 50 fps, 16,000 fps, 95,000 fps, respectively. Insets are the corresponding images. Scale bars are 100 μm, 50 μm and 10 μm, respectively. A higher frame rate is associated with a smaller field of view. In (c), the field of view reaches the lower limit, where the field of view is about 35 μm by 35 μm.

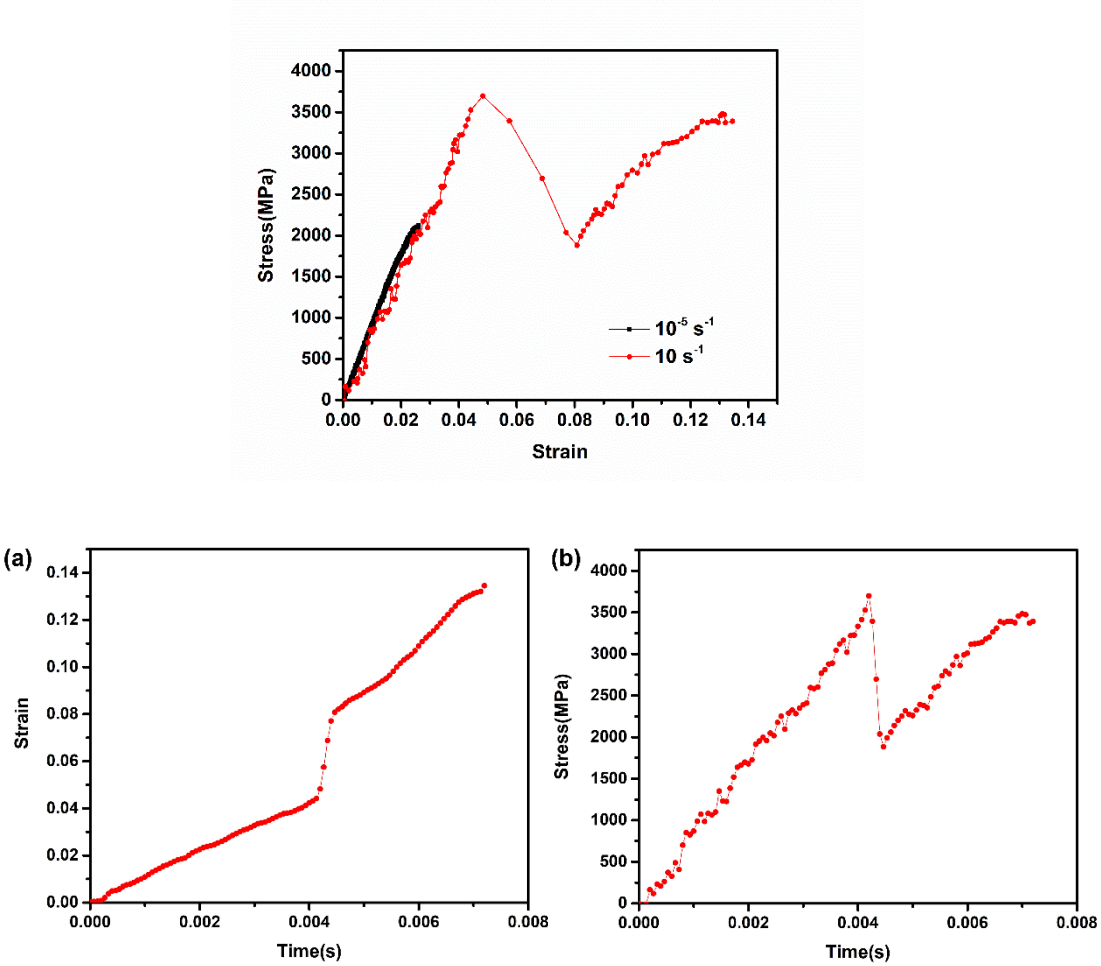

Fig. 12. (a) Stress-strain curves of the two Au nanowires tested at different strain rates. (b, c) Stress-time and strain-time curves for the Au nanowire tested at the strain rate of 10 s^{-1}.

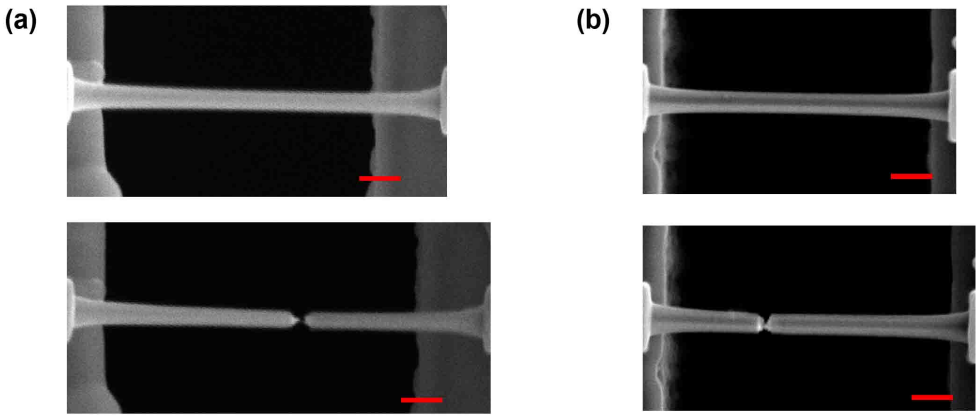

Fig. 13. SEM images of the two tested Au nanowires before and after testing. (a) 10/s. (b) 10^{-5}/s. Scale bar: 300 nm.